Advances in Applied Mathematics and Mechanics
Adv. Appl. Math. Mech., Vol. **8**, No. 1, pp. 104-116

DOI: 10.4208/aamm.2014.m642
February 2016

A High-Order Discontinuous Galerkin Method for the Two-Dimensional Time-Domain Maxwell's Equations on Curved Mesh

Hongqiang Lu[1,*], Yida Xu, Yukun Gao, Wanglong Qin and Qiang Sun

College of Aerospace Engineering, Nanjing University of Aeronautics and Astronautics, Nanjing 210016, China

Received 2 June 2014; Accepted (in revised version) 10 December 2014

Abstract. In this paper, a DG (Discontinuous Galerkin) method which has been widely employed in CFD (Computational Fluid Dynamics) is used to solve the two-dimensional time-domain Maxwell's equations for complex geometries on unstructured mesh. The element interfaces on solid boundary are treated in both curved way and straight way. Numerical tests are performed for both benchmark problems and complex cases with varying orders on a series of grids, where the high-order convergence in accuracy can be observed. Both the curved and the straight solid boundary implementation can give accurate RCS (Radar Cross-Section) results with sufficiently small mesh size, but the curved solid boundary implementation can significantly improve the accuracy when using relatively large mesh size. More importantly, this CFD-based high-order DG method for the Maxwell's equations is very suitable for complex geometries.

AMS subject classifications: 65Z05

Key words: Maxwell's equations, discontinuous Galerkin method, curved mesh, radar cross-section.

1 Introduction

In the last few decades, the finite difference time domain (FDTD) method has been widely used to solve the Maxwell's Equations in the time domain [1,2], where the stair-stepped approximation of the curved boundary is usually employed which can affect the accuracy [3], particularly for complex geometries.

Finite element methods [4] have also been tried for solving the Maxwell's equations. Some bottlenecks such as the high cost due to large matrix inversion and the continuity

*Corresponding author.
Email: hongqiang.lu@nuaa.edu.cn (H. Q. Lu)

requirement over element interfaces limited its applications in high-order cases. The Finite Volume (FV) methods [5, 6], which have been widely used in Computational Fluid Dynamics (CFD), are also suitable for solving the Maxwell's equations. However, the main disadvantage of the FV methods is their low order property, which makes it necessary to increase the number of grid elements to ensure the numerical accuracy.

Over the past decade, Discontinuous Galerkin methods [7] have received growing interests in solving time-domain Maxwell's equations because of their advantages in implementing upwinding, hp-adaptivity and parallelization. In [8], DG was used to solve the dispersive lossy Maxwell's equations in PML (Perfectly Matched Layer) regions. A spatial high-order hexahedral DG was introduced in [9], where comparisons against the FDTD and the FVTD are given. The efficiency improvement of DG by using hybrid meshes is displayed in [10]. [11] discussed Petrov-Galerkin and DG methods for both time-domain and frequency-domain electromagnetic calculations. [12] introduced a non-conforming multi-element DG for irregular geometries, where unstructured triangulation is used near objects and structured quadrangulation for the rest. [13] developed two hybridizable DG methods for time-harmonic Maxwell's equations. The convergence and superconvergence of staggered DG for Maxwell's equations on Cartesian mesh were analyzed in [14]. [15, 16] and [17] developed DG methods for Maxwell's equations in meta-materials and anisotropic materials. [18] discussed a Schwarz-type domain decomposition method when solving the 3D Maxwell's equations with DG. A *hp*-adaptivity DG was employed to perform large scale electromagnetic simulations in [19].

In this paper, we aim to apply the CFD-based high-order DG to solve the Maxwell's equations in very complex geometry cases. The paper is organized as follows. In Section 2, the CFD-based high-order DG discretization is described, where the quadrature-free implementation and parallel computing are employed to save the CPU time. In Section 3, a high-order approximation of solid boundary is introduced to approach the real geometries. Numerical results are displayed in Section 4 and the paper ends with the conclusions in Section 5.

2 High-order DG discretization of the time-domain Maxwell's equations

In the case of Transverse Magnetic (TM) wave, the 2D Maxwell's equations in the conservation form can be written as:

$$\frac{\partial \mathbf{U}}{\partial t}+\nabla\cdot\mathbf{F}(\mathbf{U})=\mathbf{S}(\mathbf{U}), \tag{2.1}$$

where

$$\mathbf{U}=\begin{bmatrix}\epsilon E_z\\ \mu H_x\\ \mu H_y\end{bmatrix},\quad \mathbf{F}(\mathbf{U})=(\mathbf{F}^x,\mathbf{F}^y)\quad\text{and}\quad \mathbf{F}^x=\begin{bmatrix}-H_y\\ 0\\ -E_z\end{bmatrix},\quad \mathbf{F}^y=\begin{bmatrix}H_x\\ E_z\\ 0\end{bmatrix}.$$

Note that ϵ and μ are constants and

$$\mathbf{S}=\begin{bmatrix}0\\0\\0\end{bmatrix}$$

in free space.

Since the Maxwell's equations read very similar to the Euler equations governing the flows of inviscid fluids, the high-order DG discretization which has been used in CFD is employed for Eq. (2.1). After multiplying a test function W, integrating over the computational domain and performing an integration by parts, the following weak form can be obtained:

$$\int_\Omega W\frac{\partial \mathbf{U}}{\partial t}d\Omega+\int_{\partial\Omega}W\mathbf{F}(\mathbf{U})\cdot\mathbf{n}d\delta-\int_\Omega\nabla W\cdot\mathbf{F}(\mathbf{U})d\Omega=0,\quad\forall W, \tag{2.2}$$

where $\partial\Omega$ is the boundary of Ω. By subdividing the computational domain Ω into the non-overlapping elements Ω_e, the semi-discrete system can be written as:

$$\frac{\partial}{\partial t}\int_{\Omega_e}W_h\mathbf{U}_h d\Omega_e+\int_{\partial\Omega_e}W_h\mathbf{F}(\mathbf{U}_h)\cdot\mathbf{n}d\delta-\int_{\Omega_e}\nabla W_h\cdot\mathbf{F}(\mathbf{U}_h)d\Omega_e=0,\quad\forall W_h, \tag{2.3}$$

where $\mathbf{U}_h$ and W_h are the pth order approximations to $\mathbf{U}$ and W and they are discontinuous over element interfaces. Assume ϕ_i, $1\le i\le N(p)$ are the basis functions, Eq. (2.3) becomes:

$$\frac{\partial}{\partial t}\int_{\Omega_e}\phi_i\mathbf{U}_h d\Omega_e+\int_{\partial\Omega_e}\phi_i\mathbf{F}(\mathbf{U}_h)\cdot\mathbf{n}d\delta-\int_{\Omega_e}\nabla\phi_i\cdot\mathbf{F}(\mathbf{U}_h)d\Omega_e=0,\quad 1\le i\le N(p). \tag{2.4}$$

The flux function $\mathbf{F}(\mathbf{U}_h)\cdot\mathbf{n}$ is replaced by a numerical flux function $\mathbf{H}(\mathbf{U}_h^-,\mathbf{U}_h^+,\mathbf{n})$, where the $\mathbf{U}_h^-$ is the internal interface state and the $\mathbf{U}_h^+$ refers to the neighbouring element interface state. The choice of the numerical flux function is not unique. In this paper, for the convenience of using the quadrature-free implementation, the simple LLF numerical flux is employed:

$$\mathbf{H}(\mathbf{U}_h^-,\mathbf{U}_h^+,\mathbf{n})=\frac{1}{2}\left[\mathbf{F}(\mathbf{U}^-)\cdot\mathbf{n}+\mathbf{F}(\mathbf{U}^+)\cdot\mathbf{n}+\alpha_{max}(\mathbf{U}^--\mathbf{U}^+)\right], \tag{2.5}$$

where the α_{max} is the maximum local eigenvalue [22].

On the far-field boundary, the non-reflecting boundary condition in CFD [7] is used, where the incoming wave is simply set to be zero. On the solid boundary, the following boundary condition [6] is employed:

$$\mathbf{n}\times E_t=0,\quad\mathbf{n}\cdot H_t=0,\quad(\mathbf{n}\times H)_B=(\mathbf{n}\times H)_R-\frac{\mathbf{n}\times[\mathbf{n}\times(E_R-E_B)]}{(\mu c)_R}, \tag{2.6}$$

where the subscript B refers to the solid boundary, R refers to the internal side on the boundary and t refers to the total value which includes the incoming and the scattering parts.

After the spatial high-order DG discretization, the following system is obtained:

$$\mathbf{M}\frac{d\mathbf{u}}{dt}=\mathbf{R}, \tag{2.7}$$

for which the 4-stage Runge-Kutta time-stepping is used to obtain the time-dependent $\mathbf{u}$.

As we all know, one significant disadvantage is the CPU time cost on the numerical computation of the integrals in Eq. (2.4) over the elements and the element interfaces. In order to accelerate the numerical simulation, the quadrature-free implementation [22] is adopted to convert the numerical integration to matrix-vector multiplication.

3 Approximation of curved solid boundary

Since RCS is sensitive to the geometry, it is necessary to adopt curved elements on solid boundary to approach the real geometry. In [21], a 3D curved geometry construction method is introduced based on the given regular mesh. In this paper, the 2D case is performed similarly.

First, the normal vector at every solid boundary node is calculated by averaging the normal vectors of the neighbouring element faces on the solid boundary (as shown in Fig. 1). Then, a third-order polynomial can be constructed to replace the original straight-line element boundary:

$$f(\xi)=a_1+a_2\xi+a_3\xi^2+a_4\xi^3, \tag{3.1}$$

which satisfies the following conditions in the reference coordinate system:

$$f(v_i)=0, \quad \frac{\partial f(v_i)}{\partial X}=n(v_i), \tag{3.2}$$

where v_i represents the vertices. Eq. (3.2) forces the curved face to pass the vertices of the original straight face and the normal vectors at the vertices to be equal to the previously averaged ones.

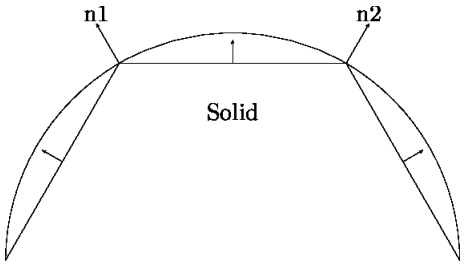

Figure 1: Evaluation of the normal vectors on solid boundary points.

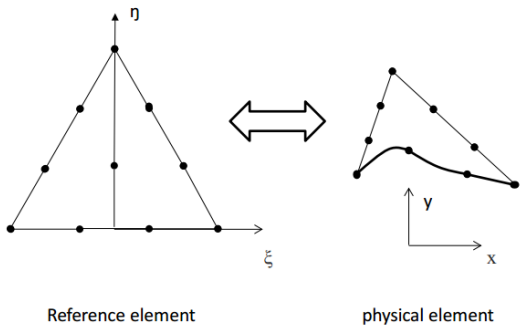

Figure 2: Mapping between physical element and the reference element.

Once the curved solid boundary is constructed, a high-order mapping between the physical element and the reference element can be obtained:

$$x = a_0 + a_1\xi + a_2\eta + a_3\xi^2 + a_4\xi\eta + a_5\eta^2 + \cdots, \tag{3.3a}$$

$$y = b_0 + b_1\xi + b_2\eta + b_3\xi^2 + b_4\xi\eta + b_5\eta^2 + \cdots, \tag{3.3b}$$

$$\xi = c_0 + c_1 x + c_2 y + c_3 x^2 + c_4 xy + c_5 y^2 + \cdots, \tag{3.3c}$$

$$\eta = d_0 + d_1 x + d_2 y + d_3 x^2 + d_4 xy + d_5 y^2 + \cdots. \tag{3.3d}$$

Fig. 2 displays the 3rd-order mapping between a physical element and the reference element.

Unfortunately, once the elements on the solid boundary are curved, the quadrature-free implementation can not be employed directly since the generated Jacobian which can be computed according to Eq. (3.3) are not constants over the curved elements. The integration over curved elements $\int_{\Omega_e}\phi_i\mathbf{U}_h d\Omega_e$ and $\int_{\Omega_e}\nabla\phi_i\cdot\mathbf{F}(\mathbf{U}_h)d\Omega_e$ are computed with numerical integration:

$$\int_{\Omega_e}\phi_i\mathbf{U}_h d\Omega_e = \sum_{ii}(\phi_i\mathbf{U}_h)_{ii}w_{ii}^{2D}|J|_{ii}^{2D}, \tag{3.4a}$$

$$\int_{\Omega_e}\nabla\phi_i\cdot\mathbf{F}(\mathbf{U}_h)d\Omega_e = \sum_{ii}(\nabla\phi_i\cdot\mathbf{F}(\mathbf{U}_h))_{ii}w_{ii}^{2D}|J|_{ii}^{2D}, \tag{3.4b}$$

where w_{ii}^{2D} are the weights of the 2D numerical quadrature integration. The integrals over the solid interfaces are calculated in the similar way:

$$\int_{\partial\Omega_e}\phi_i\mathbf{H}(\mathbf{U}_h^-,\mathbf{U}_h^+,\mathbf{n})d\delta = \sum_{ii}[\phi_i\mathbf{H}(\mathbf{U}_h^-,\mathbf{U}_h^+,\mathbf{n})]_{ii}w_{ii}^{1D}, \tag{3.5}$$

where w_{ii}^{1d} are the weights of the 1d numerical quadrature integration.

Note that only the integrals over the elements on solid boudaries and their interfaces are evaluated using numecical quadrature integration. The other integrals over the other straight-side elements and their interfaces are still computed with quadrature-free implementation which can significantly save CPU time.

4 Numerical results

The RCS distributions of several different geometries are evaluated with various grids and orders here. Particularly, The comparisons between the results obtained using curved solid boundary and straight-side solid boundary are provided.

4.1 RCS evaluation of perfectly conducting cylinder

A frequently used test case, wave scattering by a perfectly conducting cylinder in free vacuum space, is first considered, where the dimensionless TM incoming wave is given by:

$$E_z^i = \cos(2\pi(x-t)), \quad H_x^i = 0, \quad H_y^i = -\cos[2\pi(x-t)]. \tag{4.1}$$

The unstructured grids of various mesh size for the perfectly conducting cylinder are displayed in Fig. 3, where 16, 32 and 64 points are uniformly placed on the solid boundary respectively and the total number of the elements over the entire domain are 832 ($Mesh^1_{cylinder}$), 1390 ($Mesh^2_{cylinder}$) and 2504 ($Mesh^3_{cylinder}$). Note that all solid faces are curved here and all the numerical tests are performed parallely based on mesh partitioning on a single PC with multi-cores. For example, the mesh partitioning of the $Mesh^1_{cylinder}$ is demonstrated in Fig. 4.

The E_z contours at $t=5.0$ obtained on $Mesh^1_{cylinder}$ are demonstrated in Fig. 5, where the numerical accuracy is significantly improved with increasing order. Fig. 6 displays the RCS distributions obtained on the three grids with various orders. On $Mesh^1_{cylinder}$, the slight difference with the series solution can still be observed even when $p=4$ due to the large mesh size over the computational domain, especially near the solid boundary. On $Mesh^2_{cylinder}$ and $Mesh^3_{cylinder}$, the RCS solutions match well with the series solution when $p\geq 3$ and $p\geq 2$ respectively.

Fig. 7 displays the comparison of the RCS results obtained with 4th-order DG on $Mesh^1_{cylinder}$ and $Mesh^2_{cylinder}$ using curved and straight solid boundaries respectively. Significant difference can be observed when using the relatively coarse mesh $Mesh^1_{cylinder}$ since there are only 16 grid points on the solid boundary. The RCS distributions on the relatively fine mesh $Mesh^2_{cylinder}$ agree well to each other because there are more grid points placed on the solid boundary and the geometry is represented better even when using straight faces.

4.2 RCS evaluation of complex geometries

In order to demonstrate the flexibility and the robustness of the introduced DG solver, two complex cases are also tested.

First, two NACA0012 airfoils of different size are placed as shown in Fig. 8, for which the incoming wave is as same as Eq. (4.1). Note that the mesh size adopted is much larger

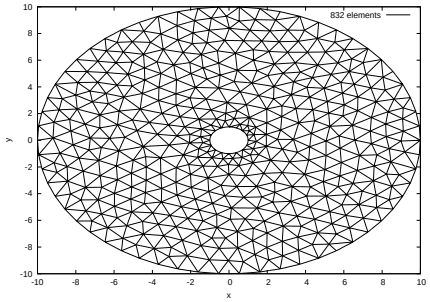

(a) Global view of $Mesh^1_{cylinder}$

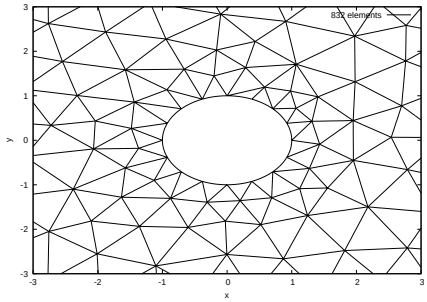

(b) Local view of $Mesh^1_{cylinder}$

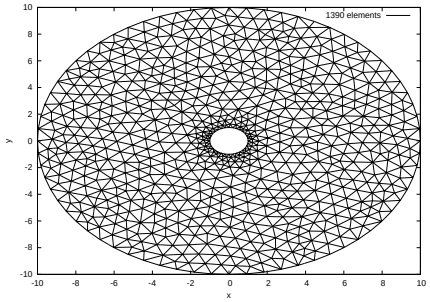

(c) Global view of $Mesh^2_{cylinder}$

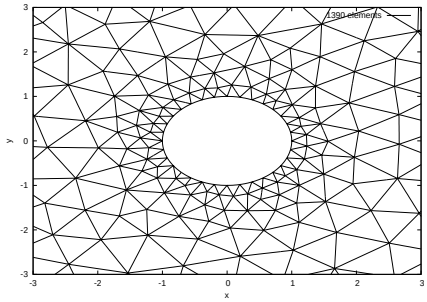

(d) Local view of $Mesh^2_{cylinder}$

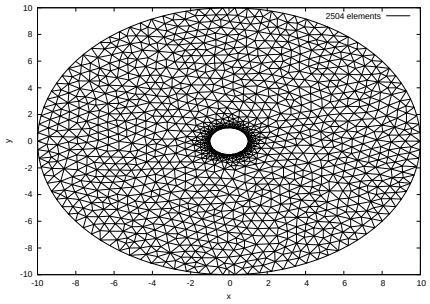

(e) Global view of $Mesh^3_{cylinder}$

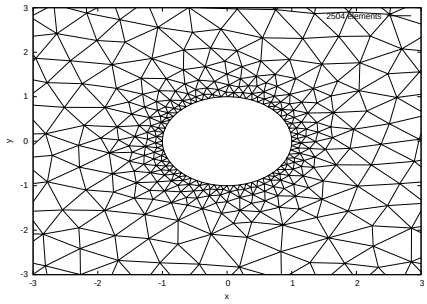

(f) Local view of $Mesh^3_{cylinder}$

Figure 3: The various grids used for perfectly conducting cylinder.

than those used in [6] since the high-order DG ($p=4$) is employed here. Fig. 9 shows the contours of E_z, H_x and H_y at $t=25.0$, which match well with those simulated using FVTD on a much finer mesh in [6]. The comparison of the RCS results obtained using high-order DG ($p=4$) and the exact controllability approach in [23] is displayed in Fig. 10, where the distributions agree well to each other.

Secondly, a more complex multi-airfoil case is tested. The computational grid is demonstrated in Fig. 11, where there are 1754 triangle elements in total and the 5th-order DG is used. The contours of E_z at $t=25.0$ are depicted in Fig. 12(a). The obtained RCS distribution in Fig. 12(b) is more complex than the others displayed above due to its

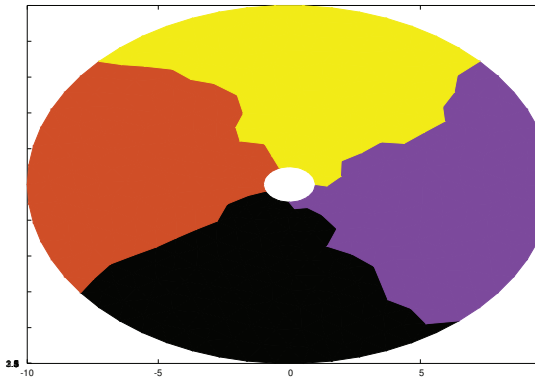

Figure 4: Mesh partitioning.

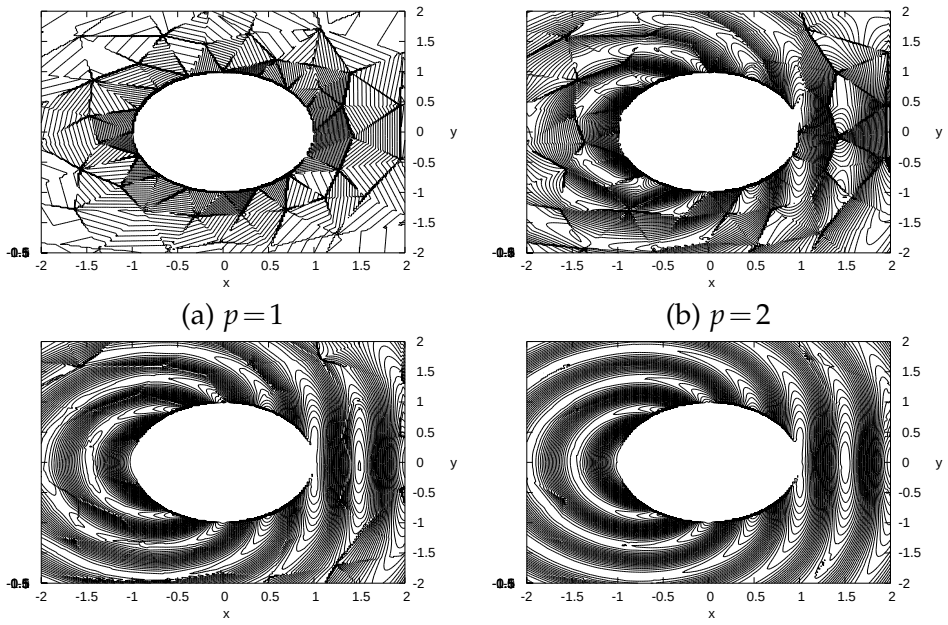

(a) $p=1$ (b) $p=2$

(c) $p=3$ (d) $p=4$

Figure 5: The E_z contours obtained using different orders on $Mesh^1_{cylinder}$.

complex geometry.

5 Conclusions

The time-domain Maxwell's equations are discretized using a discontinuous galerkin method as in CFD since they read quite similar to the Euler equations governing the flows of inviscid fluids. The quadrature-free implementation and parallel computing based on

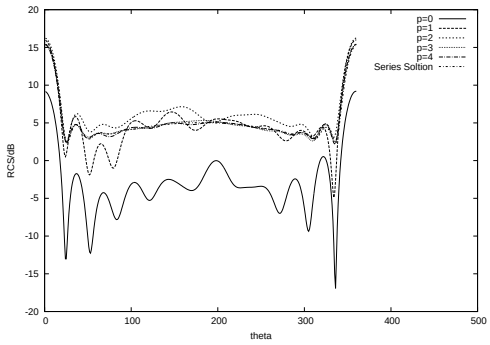

(a) RCS obtained on $Mesh^1_{cylinder}$

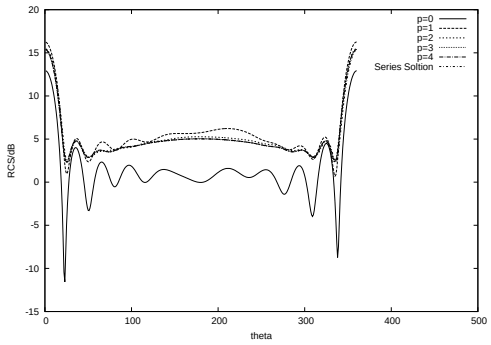

(b) RCS obtained on $Mesh^2_{cylinder}$

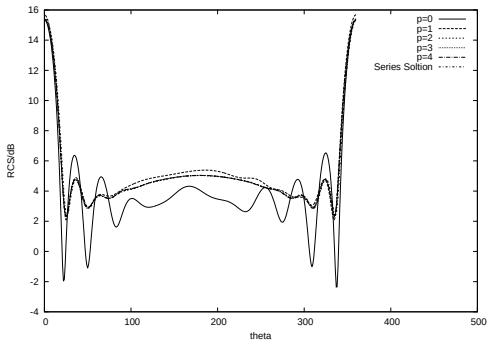

(c) RCS obtained on $Mesh^3_{cylinder}$

Figure 6: The comparison between RCS distributions.

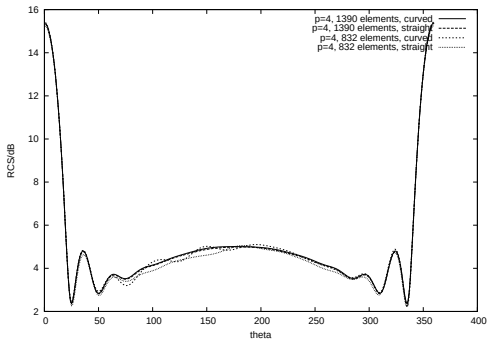

Figure 7: Comparison of the RCS results obtained using curved and straight solid boundaries.

mesh partitioning are employed to accelerate the simulation. More importantly, the solid boundaries are approximated in high-order form, which guarantees the real shapes of the geometries simulated and the accuracy of the boundary conditions. Numerical results indicate that the high-order scheme can significantly improve the numerical accu-

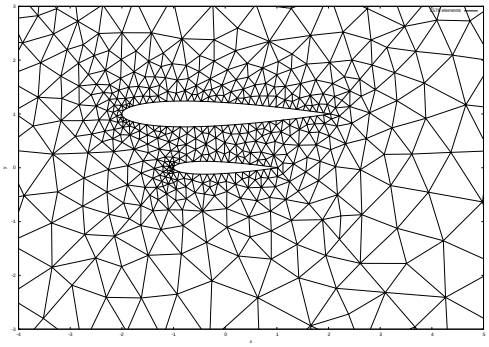

Figure 8: Mesh for double airfoil.

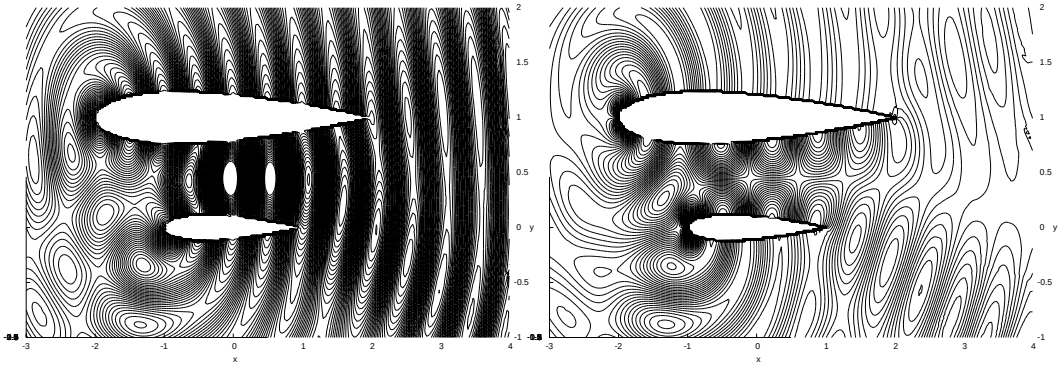

(a) E_z contours (b) H_x contours

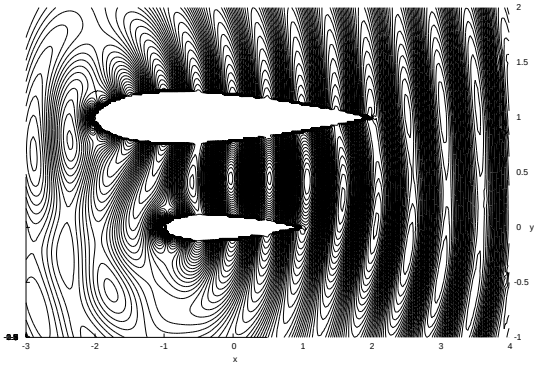

(c) H_y contours

Figure 9: The contours when $t=25.0$.

racy and the RCS is sensitive to the representation of the solid faces (curved or straight) when the mesh size near the boundary is relatively large. Furthermore, this DG solver is very suitable for complex geometries.

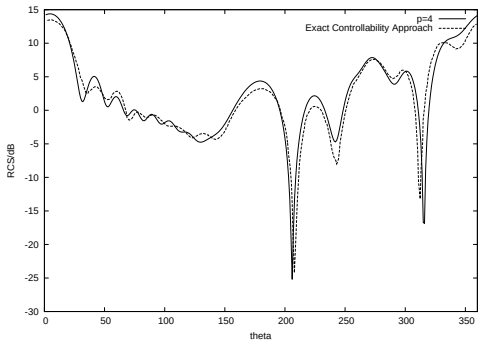

Figure 10: RCS of the double naca0012 airfoil ($p=4$).

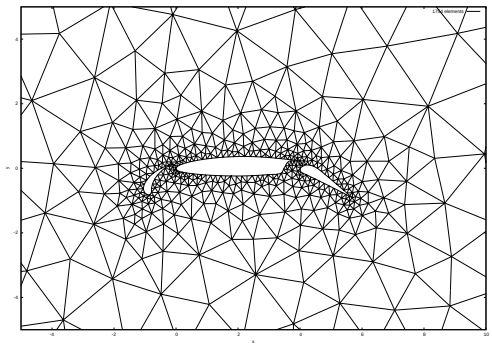

Figure 11: Mesh for multi-airfoil.

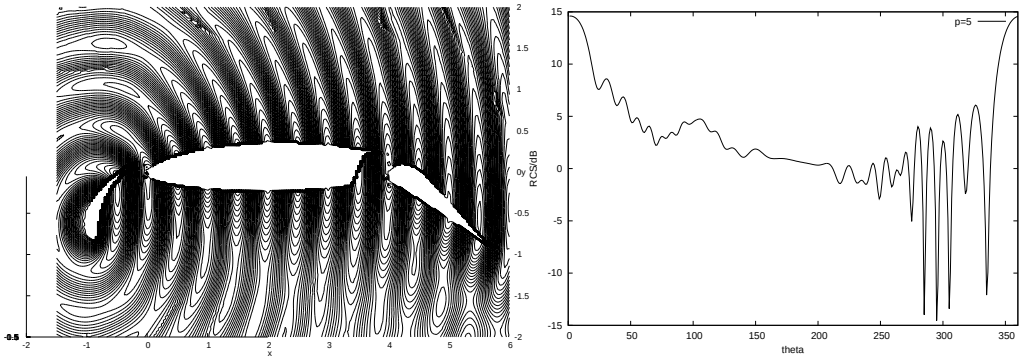

(a) E_z contours (b) RCS of the multi-airfoil

Figure 12: The E_z contours and the RCS distribution when $t=25.0$ and $p=5$.

Acknowledgements

Thanks to the National Natural Science Foundation of China: No. 11272152 and Aeronautical Science Foundation of China: No. 20101552018.

References

[1] K. S. YEE, *Numerical solution of initial value problems involving Maxwell's equation in isotropic media,* IEEE Trans. Antennas Prop., 14(3) (1966), pp. 302–307.

[2] A. TAFLOVE AND S. C. HAGNESS, Computational Electrodynamics: The Finite-Difference Time-Domain Method, Second ed., Artech, Norwood, MA, 2000.

[3] A. C. CANGELLARIS AND D. B. WRIGHT, *Analysis of the numerical error caused by the stair-stepped approximation of a conducting boundary in FDTD simulations of electromagnetic phenomena,* IEEE Trans. Antennas Prop., 39(10) (1991), pp. 1518–1525.

[4] G. COHEN AND P. MONK, *Mur-Nedelec finite element schemes for Maxwell's equations,* Comput. Meth. Appl. Mech. Eng., 169(3-4) (1999).

[5] S. PIPERNO, M. REMAKI AND L. FEZOUI, *A non-diffusive finite volume scheme for the 3D Maxwell euqations on unstructured meshes,* SIAM J. Numer. Anal., 39(6) (2002), pp. 2089–2108.

[6] Y. K. GAO AND H. Q. CHEN, *Electromagnetic scattering simulation based on cell-vertex unstructured-grid FVTD algorithm,* J. Nanjing University of Aeronautics and Astronautics, 45(3) (2013), pp. 415–423.

[7] B. COCKBURN, G. E. KARNIADAKIS AND C. W. SHU, Discontinuous Galerkin Methods: Theory, Computation and Applications, Springer, Berlin, 1999.

[8] TIAO LU, PINGWEN ZHANG AND WEI CAI, *Discontinuous Galerkin methods for dispersive and lossy Maxwells equations and PML boundary conditions,* J. Comput. Phys., 200 (2004), pp. 549–580.

[9] G. COHEN, X. FERRIERES AND S. PERNET, *A spatial high-order hexahedral discontinuous Galerkin method to solve Maxwell's equations in time domain,* J. Comput. Phys., 217 (2006), pp. 340–363.

[10] RUBEN SEVILLA, OUBAY HASSAN AND KENNETH MORGAN, *The use of hybrid meshes to improve the efficiency of a discontinuous Galerkin method for the solution of Maxwells equations,* Comput. Structures, 137 (2014), pp. 2–13.

[11] W. KYLE ANDERSON, LI WANG, SAGAR KAPADIA, CRAIG TANIS AND BRUCE HILBERT, *Petrov-Galerkin and discontinuous-Galerkin methods for time-domain and frequency-domain electromagnetic simulations,* Contents lists available at SciVerse ScienceDirect, 230 (2011), pp. 8360–8385.

[12] CLEMENT DUROCHAT, STEPHANE LANTERI AND CLAIRE SCHEID, *High order non-conforming multi-element discontinuous Galerkin method for time domain electromagnetics,* Appl. Math. Comput., 224 (2013), pp. 681–704.

[13] N. C. NGUYEN, J. PERAIRE AND B. COCKBURN, *Hybridezable discontinuous Galerkin methods for the time-harmonic Maxwell's equations,* J. Comput. Phys., 230 (2011), pp. 7151–7175.

[14] E. T. CHUNG, P. C. JR AND T. F. YU, *Convergence and superconvergence of staggered discontinuous Galerkin methods for the three-dimensional Maxwell's equations on Cartesian grids,* J. Comput. Phys., 235 (2013), pp. 14–31.

[15] JICHUN LI, *Development of discontinuous Galerkin methods for Maxwells equations in metamaterials and perfectly matched layers,* J. Comput. Appl. Math., 236 (2011), pp. 950–961.

[16] JICHUN LI, JIAJIA WANG WATERS AND ERIC A. MACHORRO, *An implicit leap-frog discontinuous Galerkin method for the time-domain Maxwells equations in metamaterials,* Comput. Methods Appl. Mech. Eng., 223-224 (2012), pp. 43–54.

[17] MICHAEL KONIG, KURT BUSCH AND JENS NIEGEMANN, *The discontinuous Galerkin Time-Domain method for Maxwells equations with anisotropic materials*, Photonics Nanostructures-Fundamentals Appl., 8 (2010), pp. 303–309.

[18] VICTORITA DOLEAN, STEPHANE LANTERI AND RONAN PERRUSSEL, *A domain decomposition method for solving the three-dimensional time-harmonic Maxwell equations discretized by discontinuous Galerkin methods,* J. Comput. Phys., 227 (2008), pp. 2044–2072.

[19] SASCHA M. SCHNEPP AND THOMAS WEILAND, *Efficient large scale electromagnetic simulations using dynamically adapted meshes with discontinuous Galerkin method,* J. Comput. Appl. Math., 236 (2012), pp. 4909–4924.

[20] MOHAMED EL BOUAJAJI AND STEPHANE LANTERI, *High order discontinuous Galerkin method for the solution of 2D time-harmonic Maxwells equations,* Appl. Math. Comput., 219 (2013), pp. 7241–7251.

[21] C. LÜBON, M. KESSLER, S. WAGNER AND E. KRMER, *High-order boundary discretization for discontinuous Galerkin codes,* 25th AIAA Applied Aerodynamics Conference, 05C08 June 2006, San Francisco, California.

[22] H. L. ATKINS AND C. H. SHU, *Quadrature-free implementation of discontinuous Galerkin method for hyperbolic equations,* AIAA J., 36(5) (1998).

[23] H. Q. CHEN AND M. K. HUANG, *Computations of scattering waves in 2-D complicated fields by using exact controllability approach,* Chinese J. Comput. Phys., 17(4) (2000), pp. 414–420.